

Earth and Space Science



RESEARCH ARTICLE

10.1029/2022EA002217

Key Points:

- Northern mid-latitude mesospheric cloud frequencies are reported from satellite observations that detect the brightest clouds there
- From 2007 to 2021 frequencies do not show a multi-year trend or a dependence on the solar cycle but show extreme interannual variability
- July frequencies correlate with interannual variations in morning rocket launches, consistent with transport of exhaust modulated by tides

Correspondence to:

M. H. Stevens,
michael.stevens@nrl.navy.mil

Citation:

Stevens, M. H., Randall, C. E., Carstens, J. N., Siskind, D. E., McCormack, J. P., Kuhl, D. D., & Dhadly, M. S. (2022). Northern mid-latitude mesospheric cloud frequencies observed by AIM/CIPS: Interannual variability driven by space traffic. *Earth and Space Science*, 9, e2022EA002217. <https://doi.org/10.1029/2022EA002217>

Received 6 JAN 2022

Accepted 23 APR 2022

Author Contributions:

Conceptualization: Michael H. Stevens
Data curation: Cora E. Randall, Justin N. Carstens
Formal analysis: Michael H. Stevens
Investigation: Michael H. Stevens, Cora E. Randall, David E. Siskind
Methodology: Michael H. Stevens, Cora E. Randall, David E. Siskind
Resources: Cora E. Randall
Software: Michael H. Stevens, Justin N. Carstens

© 2022 The Authors. This article has been contributed to by U.S. Government employees and their work is in the public domain in the USA.

This is an open access article under the terms of the [Creative Commons Attribution-NonCommercial-NoDerivs License](#), which permits use and distribution in any medium, provided the original work is properly cited, the use is non-commercial and no modifications or adaptations are made.

Northern Mid-Latitude Mesospheric Cloud Frequencies Observed by AIM/CIPS: Interannual Variability Driven by Space Traffic

Michael H. Stevens¹ , Cora E. Randall² , Justin N. Carstens³ , David E. Siskind¹ , John P. McCormack⁴ , David D. Kuhl⁵ , and Manbharat S. Dhadly¹ 

¹Space Science Division, U.S. Naval Research Laboratory, Washington, DC, USA, ²Laboratory for Atmospheric & Space Physics and Department of Atmospheric & Oceanic Sciences, University of Colorado Boulder, Boulder, CO, USA, ³Center for Space Science and Engineering, Bradley Department of Electrical and Computer Engineering, Virginia Polytechnic Institute and State University, Blacksburg, VA, USA, ⁴NASA Heliophysics Division, Science Mission Directorate, Washington, DC, USA, ⁵Remote Sensing Division, U.S. Naval Research Laboratory, Washington, DC, USA

Abstract Recent advances in data processing from the Cloud Imaging and Particle Size (CIPS) instrument on the NASA Aeronomy of Ice in the Mesosphere satellite allow observation of bright mesospheric clouds at mid-latitudes (<60°). When adjusted for the evolving local time (LT) of the CIPS observations during its mission we find that the frequencies of these bright clouds in the northern hemisphere show no trend from 2007 to 2021 and no dependence on the solar cycle, although the interannual variability is extreme. Rather we investigate the possible link with propellant exhaust from orbital vehicles, typically launched at lower latitudes. By filtering the launch record equatorward of 60°N using only those launches between 23 and 10 LT, we find a strong correlation with the observed mid-latitude mesospheric cloud frequency variability between 56° and 60°N. Meridional winds at 92 km from a meteorological analysis system reveal that these morning launches occurred at the time of maximum northward transport. Based upon this combination of high correlation between the cloud frequency and the launch record plus favorable transport conditions, it is likely that space traffic has a strong influence on the interannual variability of these bright mesospheric clouds.

1. Introduction

Polar mesospheric clouds (PMC) are comprised of water ice particles that typically form around summer solstice near 83 km and poleward of 60° latitude. Here temperatures can drop below 150 K, establishing one of the most exotic environments in the Earth's atmosphere. The mere existence of PMC makes them a compelling target for study of multi-decadal change as they are extremely sensitive to small variations in the ambient temperature and water vapor. Typically, PMC are either reported as brightness (sometimes albedo or ice water content, e.g., Hervig et al., 2016 and references therein) or as cloud frequency (e.g., Bailey et al., 2005; Russell et al., 2014). Frequency can be a particularly useful metric in quantifying their variability at mid-latitudes (<60°N), where they are much sparser.

Observations of mesospheric clouds by the naked eye are typically between 55° and 65° (Gadsden, 1998) where they are better known as noctilucent clouds (NLC). In this work, we will call them mesospheric clouds (Hervig et al., 2016) since we only use mid-latitude satellite cloud data herein. The long ground-based historical record makes them attractive as a diagnostic for decadal scale change; however, in practice, sampling and observational difficulties complicate the utilization of this record (e.g., Kirkwood et al., 2008). The geographically isolated nature of ground-based observations as well as inconsistent weather conditions necessarily raise the question as to how globally representative a given time series might be. More recently, digital cameras have allowed for a better interpretation of observed mesospheric cloud variations at mid-latitudes (Dalín et al., 2008). Nonetheless, a validated, multi-year satellite data set of mid-latitude mesospheric clouds can provide valuable context to this end.

Several case studies during the space shuttle program showed that water vapor exhaust deposited in the lower thermosphere near Florida at launch can be transported to either the Arctic or Antarctic to create bursts of PMC about a week later (Kelley et al., 2010; Stevens et al., 2003, 2005a, 2005b, 2012, 2014). These bursts were detected primarily by an increase in PMC frequency, although the cloud brightness can also measurably increase. DeLand and Thomas (2019a) recently studied the impact of all space traffic on relative changes to PMC up to

Validation: Michael H. Stevens, Justin N. Carstens, John P. McCormack, David D. Kuhl, Manbharat S. Dhadly

Visualization: Michael H. Stevens

Writing – original draft: Michael H. Stevens

Writing – review & editing: Cora E. Randall, David E. Siskind, John P. McCormack, Manbharat S. Dhadly

10 days after launches and found only a limited effect for the latitude band 65°–75°N. However, they emphasized that the small number of cloud detections at more equatorward latitudes (<65°N) prevented them from evaluating the potential link to space traffic there. Thus, the impact of space traffic on a multi-year time series of mid-latitude mesospheric cloud frequencies currently remains unquantified.

Previous studies on understanding space shuttle main engine plume observations explored the rapid transport between 100 and 110 km (Datta-Barua et al., 2021; Kelley et al., 2009; Liu, 2007; Meier et al., 2010; Niciejewski et al., 2011; Wang et al., 2017; Yue et al., 2013; Yue and Liu, 2010), since that is the altitude range where most of the shuttle water vapor exhaust is injected (e.g., Meier et al., 2011). In contrast, here we limit our analysis of horizontal winds to altitudes from 90 to 95 km to assess rapid northward transport and the resultant impact of space traffic exhaust on CIPS mid-latitude mesospheric cloud frequencies.

This work fits into the larger discipline which seeks to understand the environmental effects of emissions from space launches, including mesospheric cloud formation (Dallas et al., 2020). A recent modeling study assessing the global atmospheric response of PMC formation to launches simulated 10⁵ flights per year to determine an increase in PMC (Larson et al., 2017). In contrast, the analysis of the existing launch record presented here shows that as few as six launches per month, or even fewer, can affect the observed interannual mid-latitude mesospheric cloud frequency.

NASA's Aeronomy of Ice in the Mesosphere (AIM) mission launched in 2007 to help understand why PMC form and vary (Russell et al., 2009) and has been operating nearly continuously since then. Although AIM has provided a wealth of new results at polar latitudes, mid-latitude observations heretofore from AIM are sparse (Hervig et al., 2016). Here we present northern mid-latitude mesospheric cloud frequencies from the Cloud Imaging and Particle Size (CIPS) instrument on AIM during its years of operation (2007 to present). These CIPS results are enabled by a new algorithm (version 05.20) that better isolates the relatively weak cloud signal from the bright mid-latitude Rayleigh scattering signal observed in the nadir. The analysis is complicated by the evolving local time (LT) of the CIPS observations during its years of operation, which strongly affects the frequency time series in the most recent years of observation. Further, the threshold for detection is high at mid-latitudes; CIPS can only detect the brightest tail of the distribution here.

This study is organized as follows. We will discuss the new cloud retrieval algorithm in Section 2 and validate against concurrent mid-latitude observations in Section 3. In Section 4 we show the mid-latitude mesospheric cloud frequency time series from 2007 to 2021, as well as the total observed ice mass at mid-latitudes from one season. In Section 5 we show how a meteorological analysis system that assimilates data in the upper mesosphere can explain transport of space traffic exhaust from mid-latitudes to the sub-Arctic in a June 2019 case study. Section 6 explores how the launch LT affects the comparison of the launch record with CIPS mid-latitude cloud frequencies. Section 7 shows how we determine the phase and amplitude of the migrating diurnal and semi-diurnal tide using meridional winds from a meteorological analysis system to reconcile the selection of LT in Section 4. Section 8 summarizes some implications of these results.

2. CIPS Observations and Data Analysis

The CIPS instrument consists of four cameras that image the Earth in the nadir at 265 nm with a field-of-view that is about 2,000 km × 800 km (McClintock et al., 2009). The observations are made during the daytime at a variety of solar scattering angles, allowing for the separation of the cloud signal from the relatively bright Rayleigh scattered background. The Level 2 v5.20 data, which is used herein, has a spatial resolution of 7.5 × 7.5 km. Details on the previous version of the CIPS cloud retrievals (v04.20) may be found in Lumpe et al. (2013) and Carstens et al. (2013).

AIM is in a sun-synchronous orbit with an inclination of 97° so CIPS can observe over nearly the entire polar summer region when its field-of-view is sunlit. Earlier in the mission (2007–2015) the mid-latitude cloud observations were between 13 and 16 LT on the descending node of the AIM orbit, but for the last four seasons (2018–2021) the orbit precessed so that the mid-latitude observations were between 6 and 10 LT on the ascending node as shown in Figure 1. We will show that these changes are important in the interpretation of the time series because the cloud frequency is a strong function of LT at mid-latitudes. Operational issues prevented cloud retrievals for the northern 2017 season.

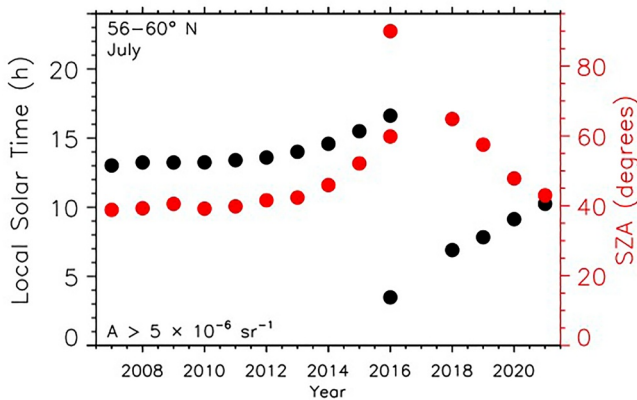


Figure 1. July averaged local solar time (in black) and solar zenith angle (SZA, in red) of CIPS cloud observations from 2007 to 2021 at latitudes from 56° to 60°N for the indicated albedo (A) threshold. Descending node observations are shown before 2016 and ascending node observations after. Data from both nodes are included during 2016, no CIPS Level 2 data are available for the 2017 cloud season, and CIPS did not make any observations in the second half of July 2019.

at higher latitudes, the number of pixels that can detect these clouds at mid-latitudes is much more limited due to the brighter Rayleigh background there. We validate the resultant CIPS mid-latitude cloud frequencies against concurrent satellite observations in the next section.

One important limitation to previous versions of the CIPS data was that clouds were not retrieved at solar zenith angles less than 40° (Lumpe et al., 2013). The new version of CIPS data is not fundamentally more sensitive at mid-latitudes; rather, the retrieval errors are now propagated through the processing, allowing disambiguation of dim clouds from false cloud detections. The latter advance is particularly important for the mid-latitudes where the clouds are typically dim and infrequent enough that biases can become significant if not properly removed.

The new algorithm accounts for the sensitivity of each pixel to detection of a cloud with a particular albedo. This is achieved by calculating the probability that a reported cloud detection in a given pixel is false, which is determined by the χ^2 distribution of the Rayleigh background removal and the pixel noise. For the work described here, any pixels for which the viewing geometry (i.e., view, scattering, and solar zenith angles) precludes accurately distinguishing between Rayleigh scattering and ice particle scattering are omitted from the analysis. We find that requiring the cloud albedo to exceed $5 \times 10^{-6} \text{ sr}^{-1}$ minimizes false cloud detections while still retaining sufficient numbers of valid measurements at latitudes from 56° to 60°N for the years considered herein (2007–2021). This relatively high threshold represents the brightest clouds in the CIPS dataset typically used for analysis. For comparison, the noise floor of the CIPS data at polar latitudes is about $2 \times 10^{-6} \text{ sr}^{-1}$ (Lumpe et al., 2013). Thus, while CIPS can observe dimmer clouds ($<5 \times 10^{-6} \text{ sr}^{-1}$)

3. Mesospheric Cloud Frequency Comparison With SHIMMER

The Spatial Heterodyne IMager for MEsospheric Radicals (SHIMMER) was launched in March 2007 into a low inclination (35.4°) orbit to measure mesospheric hydroxyl (OH) on the limb near 308 nm (Englert et al., 2010). Along with the OH observations, SHIMMER measured mid-latitude mesospheric cloud altitude profiles from 2007 to 2009 over the daytime portion of the diurnal cycle (Stevens et al., 2010). Limb viewing UV mesospheric cloud observations are typically more sensitive than nadir viewing cloud observations because they do not require the removal of the relatively bright Rayleigh scattered background present when looking at down at the earth during the day.

In June 2009 CIPS was measuring clouds at nearly the same time (13 LT) and place as SHIMMER. Figure 2 shows a map of CIPS observations as well as concurrent SHIMMER observations on 25 June 2009. For the region shown in Figure 2 SHIMMER and CIPS were observing at the same latitudes and longitudes at nearly the same LT on this day. The middle of the three SHIMMER orbits in Figure 2 shows bright clouds whereas the others do not show any clouds, which is generally consistent with the orbits of CIPS data shown. However, the brightest SHIMMER clouds in the figure at 56°N and 40°E were not detected by CIPS. We note that the SHIMMER observations at this location were made about 44 min after the CIPS observations, suggesting either that there was a phase change from vapor to ice during this time or that the clouds moved horizontally between observations.

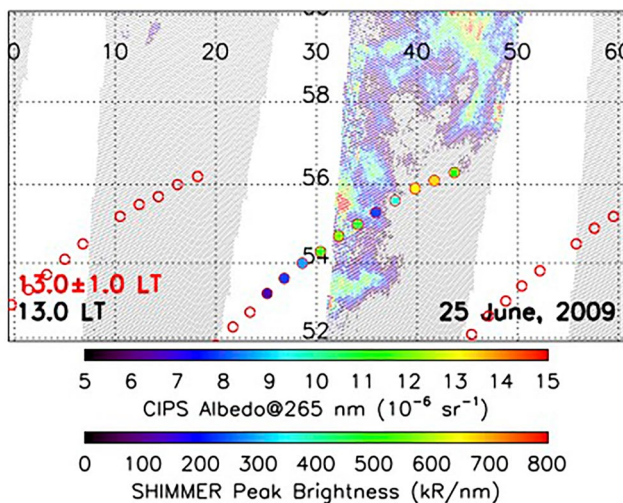


Figure 2. A region of CIPS observations on 25 June 2009. The shaded region shows pixels where observations were made and the colored region shows where clouds were observed, referenced to the color bar directly below the panel. The overplotted circles indicate where SHIMMER observations were made on the same day and same time, and are filled where a cloud was observed, referenced to the color bar at the bottom.

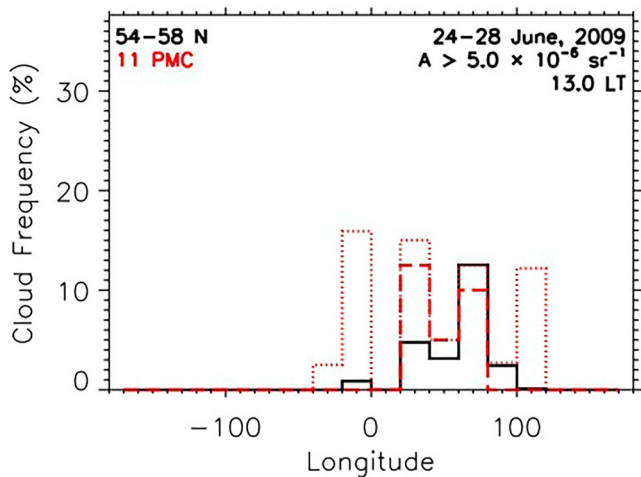


Figure 3. CIPS cloud frequency during 24–28 June 2009 in 20° longitude bins for the latitude band from 54 to 58°N (black) using the indicated cloud albedo threshold of $5 \times 10^{-6} \text{ sr}^{-1}$. SHIMMER observations of clouds during the same time period and at the same local time (LT) are overplotted in dotted red for all SHIMMER clouds observed and dashed red for the brightest SHIMMER clouds, using a threshold of 300 kR/nm. Total number of cloud profiles from the thresholded SHIMMER data is indicated.

Figure 3 assembles observations over a 5-day period from 24–28 June 2009, which includes the observations in Figure 2. The comparison is limited to 5 days because the SHIMMER observations precess in LT by about 30 min/day (Stevens et al., 2009) so this time period ensures both datasets are measuring at the same time and place. Figure 3 shows the CIPS and SHIMMER mesospheric cloud frequencies distributed into 20° longitude bins. One can see from Figure 3 that the SHIMMER frequencies are higher than CIPS, indicating a greater sensitivity to clouds by virtue of its limb viewing geometry. We therefore further sort the SHIMMER data by only taking the 29% brightest clouds, where the SHIMMER threshold of 300 kR/nm is selected so that the total frequency in Figure 3 agrees with CIPS for the indicated conditions. The resultant longitude distribution from SHIMMER in Figure 3 is in very good agreement with CIPS. Figures 2 and 3 show that the appearance of bright mid-latitude clouds are both localized in longitude and episodic, which is typical of the bright CIPS mid-latitude data as we will show. Figures 2 and 3 also reconcile the CIPS v05.20 cloud frequencies with concurrent limb viewing observations and validate further investigation of the CIPS mid-latitude cloud observations discussed in the next section.

4. Mid-Latitude Mesospheric Cloud Frequencies: 2007–2021

Figure 4 shows the July monthly averaged CIPS cloud frequencies from 56° to 60°N for 2007 through 2021. Because the LT observed by CIPS changed significantly during this time (Figure 1), we have also scaled each point in the time series in Figure 4 according to its expected frequency variation over the diurnal cycle with reference to the first season of observations in 2007. The scaling is largest near the end of the time series since frequencies peak early in the morning at mid-latitudes (see Figure 1) due to a temperature minimum in the diurnal tide at that time of day (McCormack et al., 2014; Schmidt et al., 2018). The scaling is based on the July 2009 averaged diurnal variation at mid-latitudes described by Stevens et al. (2017), who used a model that assimilated satellite temperature and water vapor data from the mesosphere as well as the bulk thermodynamic equilibrium model of Hervig et al. (2009) to infer cloud frequencies. The calculation is based on an ice water content threshold of 40 g/km², which roughly corresponds to the albedo threshold used for the time series in Figure 4 (Broman et al., 2019; Lumpe et al., 2013). The absolute frequencies calculated over the diurnal cycle by Stevens et al. (2017) range from 3% to 29% at mid-latitudes and are larger than reported from CIPS, however we only use the relative variation over the diurnal cycle to scale the data in Figure 4. The continuity of the time series in 2016 (when CIPS measurements are made on both nodes of the AIM orbit) and beyond demonstrates that the adjustment over the diurnal cycle is in the right direction by about the right amount.

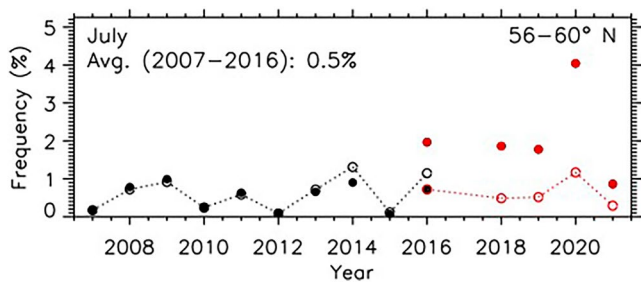


Figure 4. Interannual variability of mid-latitude mesospheric cloud frequency from 56° to 60°N for July CIPS data, using a cloud albedo threshold of $5 \times 10^{-6} \text{ sr}^{-1}$. The monthly averaged frequencies are shown in black for descending node observations (10 years average indicated) and in red for ascending node observations. No data are available for the northern 2017 cloud season. Solid symbols indicate observed monthly averaged results. Open symbols connected by the dotted line show the monthly averaged frequencies corrected for the changing local time (LT) using the diurnal variation of mid-latitude cloud frequency (see text).

The continuity of the time series in 2016 (when CIPS measurements are made on both nodes of the AIM orbit) and beyond demonstrates that the adjustment over the diurnal cycle is in the right direction by about the right amount.

Figure 4 shows many important results. The average cloud frequency for descending node observations in July is 0.5% during 2007–2016. This is lower than both the average frequency (about 5%) reported from ground-based observations near 54°N by Gerding et al. (2013) and limb viewing satellite observations near 60°N (Bailey et al., 2005), underscoring that the CIPS data presented here represent only the brightest portion of the cloud population. The average CIPS frequencies are even lower than frequencies reported from other nadir viewing observations from 50° to 64°N (about 1.5%; DeLand et al., 2007; DeLand & Thomas, 2019b). A quantitative comparison of CIPS frequencies with these results would require rigorous consideration of latitudes, longitudes, LT, days and years sampled, and sensitivity, as was done in Section 3 with SHIMMER, and is beyond the scope of this work.

In addition, there is no anti-correlation of cloud frequency with the 11 years solar cycle, which peaked in 2015 for the months shown (Machol et al., 2019).

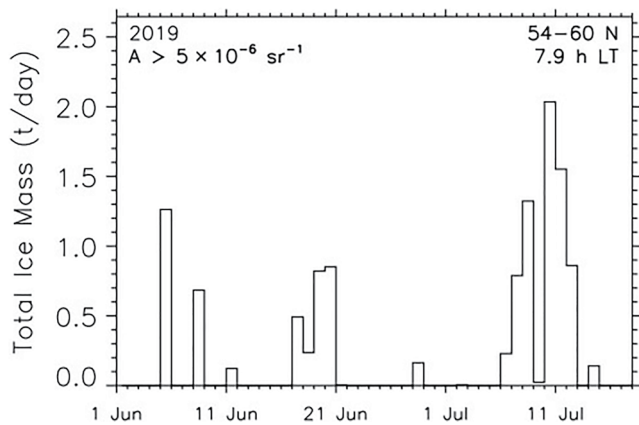


Figure 5. Total ice mass of mesospheric clouds in metric tons/day observed by CIPS during June and July 2019 from 54° to 60°N for the indicated threshold and local time (LT).

This appears to be inconsistent with ground-based observations assembled over many more years (e.g., Dalin et al., 2020; Dubietis et al., 2010; Gerding et al., 2013; Gerding et al., 2021; Kirkwood et al., 2008; Pertsev et al., 2014), as well as the change inferred by Russell et al. (2014) for these same latitudes from 2002 to 2011 using satellite temperature and water vapor data. This may be due to the high detection threshold of CIPS. However, we note that Hervig et al. (2019) reported solar cycle PMC changes to be greatly reduced after 2005 at higher latitude; this may explain why others see a solar cycle signature and we do not. Indeed, ground-based analysis of Mesospheric Summer Echoes (MSE) at 54°N between 2004 and 2017 showed no clear relationship between solar activity and MSE frequency (Pokhotelov et al., 2019).

Finally, when adjusted for the expected variation of cloud frequency over the diurnal cycle, the CIPS results in Figure 4 show no clear increase throughout the time series in the northern hemisphere from 2007 to 2021. This is consistent with results from ground-based observations over a longer time period (51 years) at the same latitudes reported by Dalin et al. (2020).

The total daily ice mass from 2019 is shown in Figure 5, which is determined from the sum of all detected ice water content (g/km^2) multiplied by the area of each CIPS pixel (56.25 km^2) for each day. We choose to show the 2019 season in more detail because it has been identified as a particularly active season for mid-latitude mesospheric clouds (Gerding et al., 2021). The variation in Figure 5 is extreme, with the daily ice mass between 0 t and 2 t. Such variability at a fixed LT motivates us to consider another source of cloud formation, so we consider here the advection of space traffic exhaust. A typical vehicle releases 100–600 tons of exhaust during a single launch (Stevens et al., 2012; DeLand & Thomas, 2019a), which is far more than shown in Figure 5 for any given day. By way of comparison with Figure 5, the response in mesospheric cloud ice mass from a space shuttle main exhaust plume in the Arctic can be 262 t/day (Stevens et al., 2005a).

5. A Case Study of Space Traffic Exhaust Forming Mid-Latitude Mesospheric Clouds

As noted above, the extreme temporal variability shown in Figures 4 and 5 leads us to consider that some mid-latitude mesospheric clouds might be produced by water vapor exhaust from space traffic. Meridional transport of space shuttle exhaust can be global in scale over a time period of days (e.g., Meier et al., 2011; Niciejewski et al., 2011; Stevens et al., 2014; Yue et al., 2013; Yue and Liu, 2010), and for the northern mid-latitudes studied here the transport is less than would be needed to reach the Arctic. Furthermore, the response to space traffic can be pronounced in cloud frequency (Stevens et al., 2003, 2005a, 2005b) and can affect the brightest subset of the clouds (Siskind et al., 2013; Stevens et al., 2012), both of which are the focus of this work. The monthly average cloud frequencies presented here are also quite low ($<1\%$, see Figure 4), so they can be more affected by water-rich exhaust plumes from lower latitudes. Furthermore, recent work has shown that the plume water vapor itself with its extremely high concentrations can locally cool the upper mesosphere to enable cloud formation, even in the polar winter (Collins et al., 2021).

We first present a parcel advection case study to show that exhaust from a June 2019 launch in Vandenberg, CA (34.7°N) can explain a burst of bright mesospheric clouds observed in the sub-Arctic a few days later. We then repeat the analysis for many different launch LT to gain insight on the relationship between launch LT and northward transport.

The parcel advection study uses meteorological fields produced by a high-altitude version of the Navy Global Environmental Model, or NAVGEM-HA (e.g., Hoppel et al., 2013; Kuhl et al., 2013; McCormack et al., 2017). NAVGEM-HA is a meteorological analysis system that assimilates data from a variety of ground-based and satellite instruments and generates atmospheric temperature, winds, and composition fields from the surface to $\sim 100 \text{ km}$ altitude globally on a 1° latitude and 1° longitude grid with a 3-hourly cadence. The winds are a product of the combined forecast model and data assimilation system and we refer to this product as “analyzed winds” hereinafter.

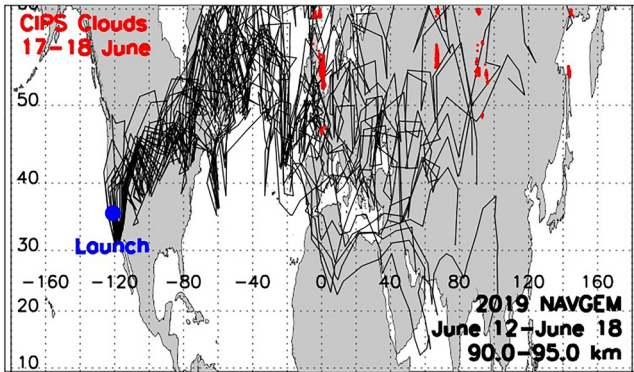


Figure 6. Parcel advection results from 90 to 95 km in 0.2 km increments following the Space-X Falcon 9 launch at 6.3 local time on 12 June 2019 from Vandenberg AFB. The initial latitude is 1°N of the launch latitude to approximate a northward launch trajectory. The locations of the CIPS clouds observed on 17–18 June are indicated in red.

increments of 0.2 km from the launch site for 6 days to infer the path of each parcel during 12–18 June. We do not consider vertical motion in this simulation and assume that horizontal motion at any given altitude is on the same pressure surface for each path. Vertical winds are highly variable and on average relatively weak (<10 cm/s) in this altitude region so that the net effect on the fate of a parcel from mid-latitudes over the time periods considered herein is small. Each parcel is treated as a passive tracer and advected in three-hour increments to be consistent with the cadence of the NAVGEM-HA output.

Figure 6 shows that on average from 90 to 95 km the meridional winds are northward and the zonal winds eastward for the time period considered. The eastward motion is largely controlled by the mean zonal wind (e.g., Yue et al., 2013). For the meridional motion, the parcels travel along similar paths early in the simulation but then diverge and ultimately spread over a wide range of latitudes including the sub-Arctic. Such rapid poleward transport has been observed before in case studies of the space shuttle main engine plume (Stevens et al., 2003, 2005a, 2005b). Previous studies have also shown that photolysis of space shuttle plume water vapor in the mesosphere and lower thermosphere (MLT) is relatively unimportant over the time scales considered here so that 73% remains after 3.4 days (Stevens et al., 2003, 2005b).

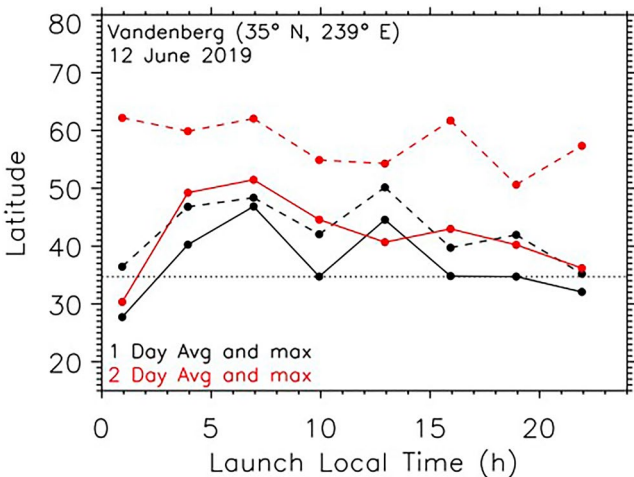


Figure 7. Latitudes of air parcel trajectories calculated for altitudes from 91 to 93 km in 0.2 km increments. Maximum (dashed) and average (solid) latitude of advected parcels from Vandenberg after 1 (black) and 2 (red) days starting on 12 June 2019. Vandenberg latitude (35°N) indicated by the dotted black line.

NAVGEM-HA output is only available for limited time periods during a few different years of the AIM mission, but one of those periods is the month of June 2019 when CIPS was observing mesospheric clouds at mid-latitudes as shown in Figure 5. NAVGEM-HA uses concurrent satellite and ground-based mesospheric and lower thermospheric temperature observations to derive vector winds so is therefore representative of the specific conditions during the time period simulated. NAVGEM-HA horizontal winds have been reliably validated up to 95 km altitude (McCormack et al., 2017; Stober et al., 2020) so we limit our analysis to the 90–95 km region where meridional winds are relatively fast and temperatures relatively low and close to the frost point. Note that below 90 km we find no evidence of rapid meridional transport to the sub-Arctic from the available NAVGEM-HA output.

We first consider the mesospheric cloud observations of 17–18 June as shown in Figure 5. In addition, Gerding et al. (2021) recently reported an unusually bright NLC on 17 June from a German ground-based station. A review of the launch record (www.spaceflightnow.com/launch-log) shows a Space-X Falcon 9 launch from Vandenberg Air Force Base (35°N, 121°W) in California at 6.3 LT of 12 June that year. Using the horizontal winds from 90 to 95 km from NAVGEM-HA, we advect parcels horizontally in altitude

increments of 0.2 km from the launch site for 6 days to infer the path of each parcel during 12–18 June. We do not consider vertical motion in this simulation and assume that horizontal motion at any given altitude is on the same pressure surface for each path. Vertical winds are highly variable and on average relatively weak (<10 cm/s) in this altitude region so that the net effect on the fate of a parcel from mid-latitudes over the time periods considered herein is small. Each parcel is treated as a passive tracer and advected in three-hour increments to be consistent with the cadence of the NAVGEM-HA output.

Significantly, some of the paths in Figure 6 are consistent with the location of the CIPS mesospheric cloud observed on 17–18 June and the NLC observed in Germany (54.1°N, 11.8°E) on 17 June. The mesospheric clouds observed by CIPS on 17–18 June represents only about 1 ton of water ice (Figure 5), which is far less than the propellant available from either the first or second stage of the Falcon 9 (100–400 tons). The altitudes used in the simulation are also close to the mesopause, where the relatively low temperatures are more likely to enable cloud formation, particularly as the parcels approach the polar summer. The advected parcels, the observed mass of the clouds, and the temperature therefore together plausibly connect the enhanced cloud activity on 17–18 June with the launch on 12 June.

Yue and Liu (2010) argued that the phase of the migrating tide may play a role in the fate of a space shuttle plume. To assess the possible impact of launch LT on the plume fate we show in Figure 7 results from eight different LT for the same day, one simulation for each three-hour time increment of NAVGEM-HA. For each simulation, Figure 7 shows both the mean and maximum latitude of each from 90 to 95 km after 1 day and after 2 days. It is crucial to assess transport of the plume in this way because the detected

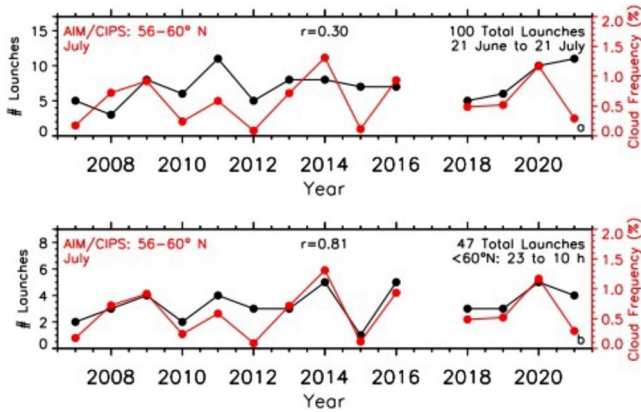


Figure 8. (a) The diurnally adjusted July averaged CIPS mesospheric cloud frequency from Figure 4 (in red) compared against the number of launches for each month (in black). The launch totals are taken 10 days prior (21 June to 21 July) to the CIPS cloud frequencies to account for transport to the sub-Arctic and cloud formation (see text). (b) Same as Figure 8a except only those vehicles launched between 23 local time (LT) and 10 LT are included for launches equatorward of 60°N. Launches poleward of 60°N are from 30 June to 30 July. The correlations between cloud frequencies and the launch record are given at the top of each panel.

cloud ice mass is so low that even small portions of the plume can contribute to the mass shown in Figure 5. It is notable that some parcels readily reach the sub-Arctic after 2 days, regardless of the launch LT. Even the average latitude of the parcels reach 50°N for early morning launches after 2 days for this time period, so the launch LT can make a difference in the ultimate latitude for the results in Figure 7. We explore this further in the next section.

6. Mid-Latitude Mesospheric Clouds and the Launch Record

To better quantify the impact of launch LT, we compare the launch record against the 14 years of CIPS data corrected for the diurnal variation of mid-latitude mesospheric cloud frequency as shown in Figure 4. We first assemble launches during each year of the CIPS observations without regard to launch LT and compare directly against the time series of mid-latitude frequencies in Figure 8a. Here we apply transport time of 10 days earlier (21 June–21 July) than the data from the July cloud observations, roughly consistent with the maximum time of response of PMC from previous case studies of the space shuttle main engine plume (Stevens et al., 2003, 2005a). For launches poleward of 60°N we use a response time of 1 day. Overall, the correlation between the launch record and the CIPS frequencies ($r = 0.30$) is not compelling.

However as shown in Figure 8b, when we restrict the selection of launches at latitudes less than 60°N to only use those greater than 23 LT or less than 10 LT, the correlation between launch record and CIPS frequencies is now excellent ($r = 0.81$). We use all launches at latitudes greater than 60°N without regard to launch LT in Figure 8b, since there is no need for northward transport to the sub-Arctic. The LT window between 23 LT and 10 LT for launches equatorward of 60°N is chosen to maximize the correlation of the CIPS frequencies with the launch record. This maximum correlation is found by testing both the width of the LT window (11 hr in Figure 8b) as well as the center of the LT window (4.5 LT) and is discussed further in Section 7. The morning time window is generally consistent with our results shown in Figure 7. It is also generally consistent with observational studies of space shuttle main engine exhaust plumes, showing that the plumes tended to travel north when launched in the morning and south when launched in the late afternoon and evening (Siskind et al., 2003; Stevens et al., 2014). Figure 8b is compelling evidence that July launches worldwide are helping to control the interannual variability of the bright mesospheric clouds observed by CIPS in the sub-Arctic. Table 1 shows all of the launches (47) used in Figure 8b time series by date and Table 2 shows the distribution by launch site latitude.

The idea that space traffic can control the interannual variability of CIPS cloud frequencies was first proposed by Siskind et al. (2013) based on data from the Arctic during 2007–2012. For this shorter time series, they found a frequency peak in 2011 that was consistent with an increase in space traffic as also shown in Figure 8. In addition, similar to what is shown in Figure 8, they found 2007 Arctic cloud frequencies observed by CIPS were lower than 2008 frequencies. In that work, they showed that 2007 temperatures in the winter polar stratosphere were unusually high and that such a deviation can drive temperatures in the polar summer mesosphere high enough to suppress cloud formation. Those CIPS data were taken from 66° to 71°N, used a lower detection threshold of $2 \times 10^{-6} \text{ sr}^{-1}$, and registered frequencies in the 20%–35% range. By contrast, here for the much smaller population of bright clouds seen by CIPS at mid-latitudes, it appears that the launch record sorted by LT in Figure 8b can explain the 2007 frequency minimum as well as subsequent maxima (2009, 2011, 2014, 2016, and 2020) and minima (2010, 2012, and 2015). We therefore find that although a link to the winter stratosphere could play a role in the interannual variability for the larger population at higher latitudes, it is not needed to explain the interannual variability of the CIPS frequencies at mid-latitudes.

It is notable that none of the launches in Table 1 include a space shuttle. Transport of the shuttle exhaust in previous studies was inferred near 105 km and created PMC at higher latitudes (>65°N). In contrast, in this work we determine transport from analyzed winds at lower altitudes (90–95 km) and to lower latitudes (56–60°N).

Table 1
Successful Orbital Launches Used in Figure 8b Time Series

Year	Date	UT	Lat	Lon	LST	Site	Vehicle
2007	02 Jul	1938	62.9	40.5	22.3	Plesetsk	Kosmos
2007	07 Jul	0116	46	63	5.5	Baikonur	Proton
2008	26 Jun	2359	46	63	4.2	Baikonur	Proton
2008	22 Jul	0240	62.9	40.5	5.4	Plesetsk	Kosmos
2008	26 Jul	1831	62.9	40.5	21.2	Plesetsk	Soyuz
2009	21 Jun	2150	46	63	2	Baikonur	Zenit
2009	30 Jun	1910	46	63	23.4	Baikonur	Proton
2009	06 Jul	0126	62.9	40.5	4.1	Plesetsk	Rokot
2009	21 Jul	0357	62.9	40.5	6.7	Plesetsk	Kosmos
2010	21 Jun	0214	46	63	6.4	Baikonur	Dnepr
2010	12 Jul	0352	13.6	80.3	9.2	Satish Dhawan	PSLV
2011	13 Jul	0227	46	63	6.6	Baikonur	Soyuz
2011	15 Jul	2316	46	63	3.5	Baikonur	Proton
2011	16 Jul	0641	28.5	-80.5	1.3	Cape Canaveral (CC)	Delta
2011	18 Jul	0231	46	63	6.7	Baikonur	Zenit
2012	29 Jun	1315	28.5	-80.5	7.9	CC	Delta
2012	15 Jul	0240	46	63	6.9	Baikonur	Soyuz
2012	28 Jul	0135	62.9	40.5	4.3	Plesetsk	Rokot
2013	01 Jul	1811	13.6	80.3	23.5	Satish Dhawan	PSLV
2013	19 Jul	1300	28.5	-80.5	7.6	CC	Atlas V
2013	19 Jul	2337	37.5	112.6	7.1	Taiyuan	Chang Zheng
2014	30 Jun	0422	13.6	80.3	9.7	Satish Dhawan	PSLV
2014	02 Jul	0956	34.8	-120.6	1.9	Vandenberg	Delta
2014	03 Jul	1243	62.9	40.5	15.4	Plesetsk	Rokot
2014	14 Jul	1515	28.5	-80.5	9.9	CC	Falcon 9
2014	18 Jul	2050	46	63	1	Baikonur	Soyuz
2015	03 Jul	0455	46	63	9.1	Baikonur	Soyuz
2016	22 Jun	0355	13.6	80.3	9.3	Satish Dhawan	PSLV
2016	24 Jun	1430	28.5	-80.5	9.1	CC	Atlas V
2016	07 Jul	0136	46	63	5.8	Baikonur	Soyuz
2016	16 Jul	2141	46	63	1.9	Baikonur	Soyuz
2016	18 Jul	0445	28.5	-80.5	23.4	CC	Falcon 9
2018	29 Jun	0942	28.5	-80.5	4.3	CC	Falcon 9
2018	09 Jul	2058	28.2	102	3.8	Xichang	Chang Zheng
2018	09 Jul	2151	46	63	2	Baikonur	Soyuz
2019	24 Jun	1809	28.2	102	1	Xichang	Chang Zheng
2019	25 Jun	0630	28.6	-80.6	1.1	Kennedy Space Center	Falcon Heavy
2019	10 Jul	1714	62.9	40.5	19.9	Plesetsk	Soyuz
2020	23 Jun	0143	28.2	102	8.5	Xichang	Chang Zheng
2020	04 Jul	2344	41.3	100.3	6.4	Jiuquan	Chang Zheng
2020	06 Jul	0100	31.9	34.7	3.3	Palmachim	Shavit
2020	15 Jul	1346	37.8	-75.5	8.7	Wallops	Minotaur
2020	19 Jul	2158	30.4	131	6.7	Tanegashima	H-IIA

Table 1
Continued

Year	Date	UT	Lat	Lon	LST	Site	Vehicle
2021	29 Jun	2327	46	63	3.7	Baikonur	Soyuz
2021	30 Jun	1447	35	-118.1	6.9	Mojave Air and Space Port	LauncherOne
2021	04 Jul	2328	41.3	100.3	6.2	Jiuquan	Chang Zheng
2021	19 Jul	0019	28.2	102	7.1	Xichang	Chang Zheng

Note. Only launches between 23 local time (LT) and 10 LT are included from mid-latitude sites (<60°N). All launches from Plesetsk (63°N, italicized) are included from 30 June through 30 July for each year. Mid-latitude launches are from 21 June through 21 July. Solid fueled launch vehicles are underscored due to less water vapor expected for that propellant (Siskind et al., 2003). There is no CIPS data from 2017, so that year is skipped. There are no launches listed after 17 July 2019 for that year due to operational issues with the AIM satellite.

Figure 8 does not consider size of launch vehicle (e.g., Stevens et al., 2012), launch site latitude (Table 2), ascent trajectory, or the water vapor yield of the propellant combination which requires additional study that is beyond the scope of this work. On the other hand it should be emphasized that water vapor mixing ratios from a single plume can be near unity (e.g., Collins et al., 2021 and references therein) and are many orders of magnitude larger than ambient mixing ratios, which are typically reported in parts per million at these altitudes. Figures 8a and 8b provide evidence that the migrating tides (i.e., those that follow the sun) contribute importantly to the northward transport of space traffic exhaust during the summer. In the next section we analyze meridional winds from high-altitude meteorological analysis systems over several years during the AIM mission to better quantify the launch LT dependence on mesospheric cloud formation indicated by Figure 8.

7. Transport to the Sub-Arctic: Migrating Tides and Diffusive Spreading

This section explores analyzed meridional wind fields to quantify the most important tidal components contributing to northward transport of space traffic exhaust to the sub-Arctic. The intent of this analysis is to reconcile apparent relationship between launch LT and CIPS cloud frequencies implied by Figure 8b with the representative MLT migrating diurnal and semi-diurnal tides in June and July. For this we include results from an additional forecast-assimilation system: Navy Operational Global Atmospheric Prediction System—Advanced Level Physics High Altitude (NOGAPS-ALPHA; Eckermann et al., 2009; Hoppel et al., 2008). The standard NOGAPS-ALPHA product (Eckermann et al., 2009) produced a meteorological analysis every 6 hours. In order to resolve the semi-diurnal tide, Siskind et al. (2012, 2014) described a product which initialized forecasts every 6 hours but provided output every hour. This hourly product, available for the summer of 2009, has been used to study a wide range of tidal modes (Lieberman et al., 2015; Stevens et al., 2017).

Following the work of Yue and Liu (2010), the most important components contributing to poleward transport are the diurnal migrating tide, the semi-diurnal migrating tide, and the quasi-two-day wave (Q2DW). Some non-migrating tides and other planetary waves will be present but we herein limit the analysis to those modes expected to contribute to transport over thousands of kilometers in days to weeks. We focus primarily on the altitudes from 91 to 93 km and on the latitude and longitude of Cape Canaveral (28°N and 279°E), which is one of the most active launch sites in the world (Table 2).

The three components above are simultaneously fit using a least-squares algorithm for the desired latitude or longitude gridpoint and for each altitude up to 95 km. For every timestep throughout the 21 June to 21 July time period and at each altitude, we use an 8-day window (4 days on either side) and save the amplitude and phase of a diurnal oscillation, a semi-diurnal oscillation, the Q2DW, as well as the mean meridional wind for the middle of the 8-day window. The next timestep (hourly for 2009 or 3-hourly for the other years which use the NAVGEM analysis) is fit and so on until the end of the time period so that the resulting time series of components is implicitly smoothed over 8 days. The explicit expression fit to the NAVGEM-HA and NOGAPS-ALPHA meridional wind output is

$$v(z, t) = v_0(z, t) + A_{48}(z, t) \cos \left[\left(\frac{2\pi}{48} \right) (t_{48} - \phi_{48}(z, t)) \right] + A_{24}(z, t) \cos \left[\left(\frac{2\pi}{24} \right) (t_{24} - \phi_{24}(z, t)) \right] + A_{12}(z, t) \cos \left[\left(\frac{2\pi}{12} \right) (t_{24} - \phi_{12}(z, t)) \right] \quad (1)$$

Table 2
Number of Launches From Each Site in Table 1 Sorted by Latitude

Number	Location	Latitude
8	Plesetsk	62.9 N
15	Baikonur	46.0 N
2	Jiuquan	41.3 N
1	Wallops	37.8 N
1	Taiyuan	37.5 N
2	Vandenberg/MHV	34.8 N
1	Palmachim	31.9 N
1	Tanegashima	30.4 N
8	CC/KSC	28.5 N
4	Xichang	28.2 N
4	Satish Dhawan	13.6 N
47	Total	

Note. Cape Canaveral (CC) and the Kennedy Space Center (KSC) are taken to be at the same location. Vandenberg and MHV are taken to be at the same location.

where $v_0(z,t)$ is the mean meridional wind at altitude z and time t (in h), $A(z,t)$ is the amplitude of the Q2DW (A_{48}), the diurnal tide (A_{24}), or the semi-diurnal tide (A_{12}), and $\phi(z,t)$ (in h) is the corresponding phase of the same three components. The tidal oscillations are calculated at the center of the sliding 8-day window with a period of 48 hr for the Q2DW (t_{48}) or 24 hr for the diurnal and semi-diurnal tide (t_{24}). Our approach therefore does not fit a wavenumber to the oscillations but rather quantifies the temporal variation of the above oscillations at a single spatial gridpoint in order to minimize the averaging required to fit the data. Thus, for example, non-migrating and migrating components are mixed together in these results. This approach is driven by the specific geographic location of the launch site and the observed rapid, global-scale transport of space traffic exhaust over many latitudes which demands as little averaging as possible (see Figure 6). However, previous studies have readily shown that the wavenumber 1 migrating diurnal tide (DW1) and the wavenumber 2 migrating semi-diurnal tide (SW2) are typically the strongest modes for the altitudes, latitudes, and season considered here (e.g., Forbes, 1995; Oberheide et al., 2009; Wu et al., 2008a, 2008b; 2011).

An example of the NOGAPS-ALPHA output and the composite fit for 1 month is shown in Figure 9 at 91.4 km altitude near Cape Canaveral (29°N, 279°E) from the NOGAPS-ALPHA system in 2009. The data are averaged over ± 2 latitude gridpoints north and south of Cape Canaveral as well as ± 2 longitude gridpoints east and west. When using the more finely sampled NAVGEM-HA product this averaging is over ± 3 longitude gridpoints. This

helps to reduce the variability while maintaining the main features of the temporal oscillations. Here we have also overplotted results for the same latitude and months from the horizontal wind model (HWM14) which is an empirical model often used in this region of the atmosphere (Drob et al., 2015). The extreme day-to-day variability in the analyzed meridional winds is evident as is the significant underestimate of HWM14, which can be expected from a climatology. Also overplotted is the reconstructed fit using all components which captures the amplitude and phase of the main features, although even the composite fit cannot resolve the peaks and troughs of the analyzed winds. Nonetheless, the reconstructed fit is adequate to assess the phases and variability of the components, which are the focus of this section. Figure 10 shows the same data but over a shorter time period (8 days) to more clearly show the peak-to-trough variability of the data and the reconstructed fit. Figure 10 also shows the three individual components split out from the composite fit, with the amplitude of each indicated.

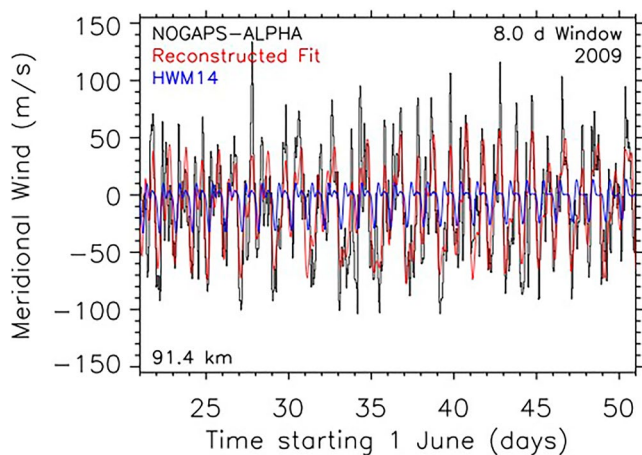


Figure 9. NOGAPS-ALPHA analyzed meridional winds for 21 June to 21 July 2009 over Cape Canaveral, FL (29°N, 279°E). Overplotted is the reconstructed fit (red) as well as HWM14 empirical model at 91.4 km (blue) for the same time period and latitude.

Figure 11a shows the derived amplitudes of the three components used in Figures 9 and 10 over all days considered in this study. All of them contribute, but the diurnal migrating tide is most often the strongest for the location, time period, and altitude shown. Also shown in Figure 11a is the mean wind (v_0 in Equation 1), which is on average southward at 10.6 m/s and typical of the mean meridional wind in this region of the atmosphere for the indicated time period. Net northward transport of any tracer therefore needs to overcome this through a combination of the tidal modes present and diffusive spreading. Figure 11b shows the LT of the maximum northward wind for the diurnal and semi-diurnal components from the output in Figure 11a, which are consistently near the indicated means of 11.2 and 2.2 hr.

Figures 12a–12c show the altitude dependence of the amplitudes for the semi-diurnal component, the Q2DW, and the diurnal component, respectively, averaged between 21 June and 21 July for five different years during the AIM mission. In each case the monthly averaged mean wind is also shown for comparison. Derived amplitudes of the semi-diurnal tide in Figure 12a are consistent with the independent analysis of 2010 NAVGEM-HA output by Stober et al. (2020). Amplitudes of the semi-diurnal tide, diurnal tide, and mean wind are similar to July 1993 zonal averages from 90 to 95 km derived

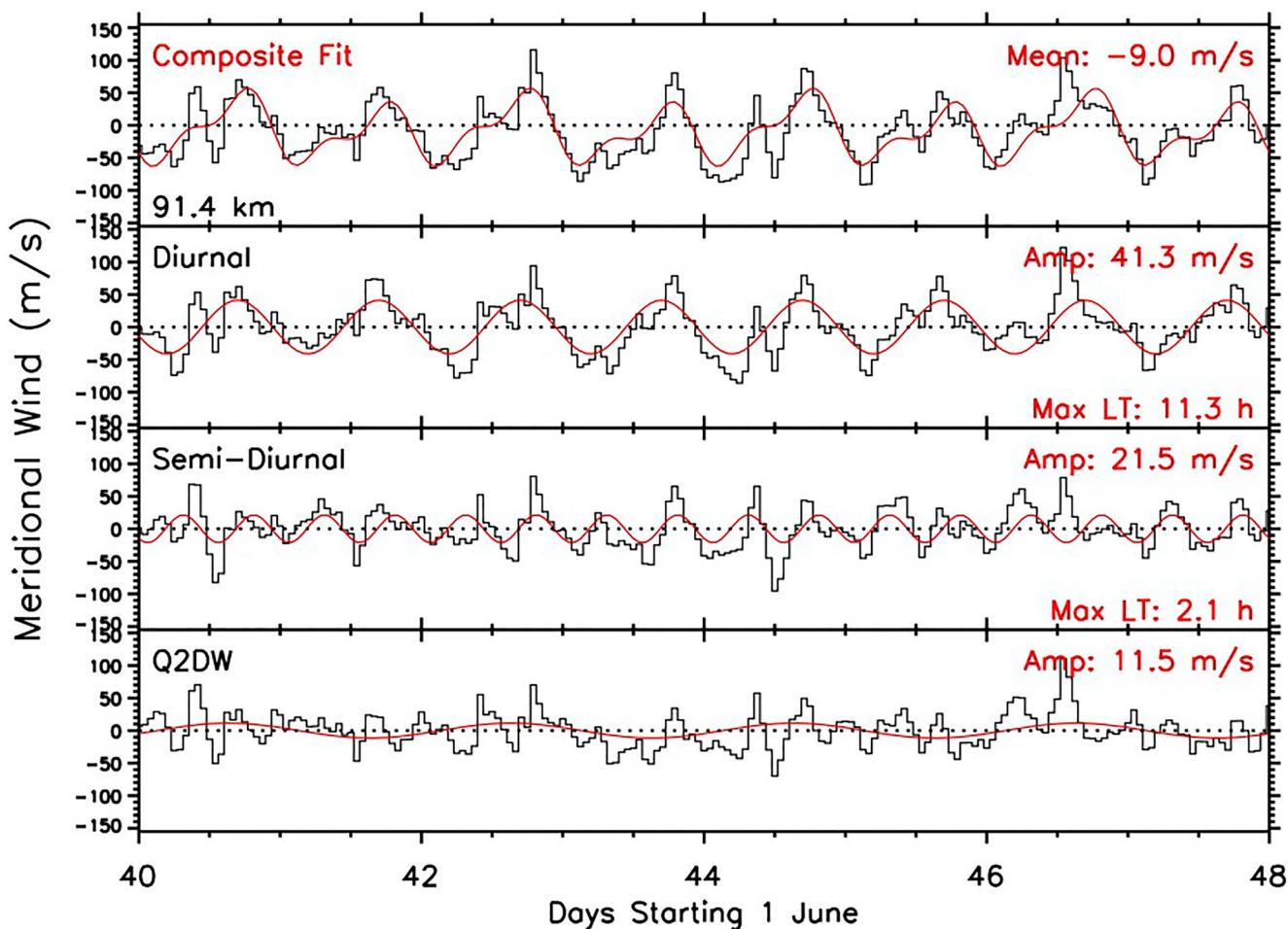


Figure 10. (top) Analyzed winds (black) for a sample 8-day fitting window from Figure 9 (without HWM14) along with the composite fit (red). Each of the fitted components is shown separately in the panels below. The black histogram of each component represents the analyzed winds with the other two components subtracted. The fitted solution to each component is shown in red.

using data from the Wind Imaging Interferometer (WINDII) on the NASA TIMED satellite (Zhang et al., 2007). Amplitudes of the migrating diurnal tide and the Q2DW are consistent with results from McCormack et al. (2014) using the 2009 NOGAPS-ALPHA 6-hourly product. Figure 12 serves to illustrate that the amplitudes are on average representative for the AIM years of operation and that all three components as well as the mean wind

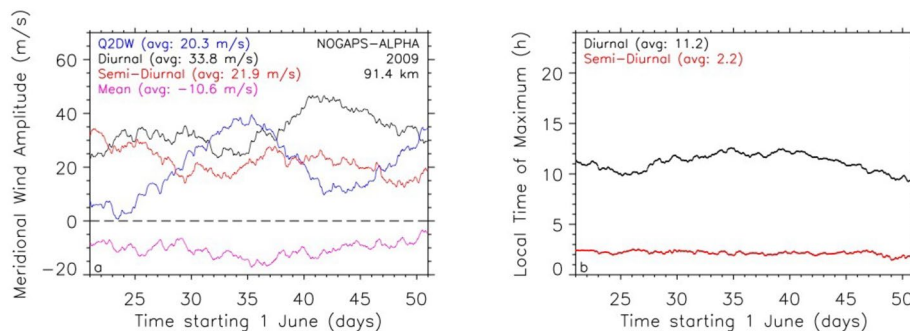


Figure 11. (a) Derived amplitudes at 91.4 km for the diurnal tide, semi-diurnal tide, and the Q2DW over Cape Canaveral during the time period of interest in 2009. Also shown is the derived mean wind. Monthly averages for each component are indicated in the upper left. (b) Corresponding LT of maximum northward wind for the diurnal and semi-diurnal components in (a) during the same time period, with the monthly averages indicated.

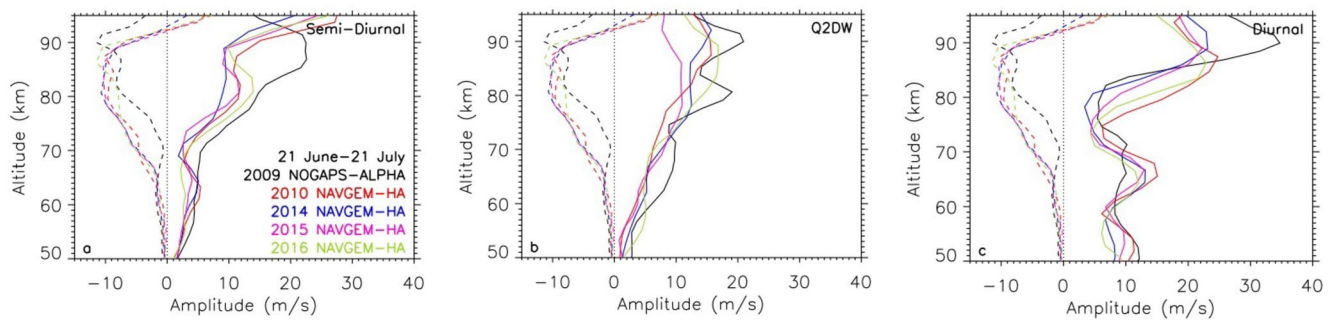


Figure 12. (a) Altitude dependence of the semi-diurnal component meridional wind amplitude over Cape Canaveral for the time period of this study (21 June to 21 July) and for 5 different years of NOGAPS-ALPHA and NAVGEM-HA analyzed winds (solid lines). The NOGAPS-ALPHA or NAVGEM-HA mean wind is shown as the dashed lines. (b) Same except for the Q2DW. (c) Same except for the diurnal component.

contribute to the meridional motion of a parcel. The NOGAPS-ALPHA semi-diurnal tidal amplitude has a different altitude dependence above 90 km in Figure 12 and the NOGAPS-ALPHA diurnal amplitude is larger above 90 km. Importantly, however, the components for all years are largest near the top altitudes (90–95 km) where we have run our parcel advection simulations in Figures 6 and 7.

Although the altitude dependence of the components shown in Figure 12 is instructive, the meridional transport is also described by the variation of these components with latitude between 29°N and 56°N. In this part of the analysis, we only consider the NAVGEM-HA analyzed winds because these have been validated with independent ground-based observations (McCormack et al., 2017; Stober et al., 2020) whereas the NOGAPS-ALPHA winds have not. To explore this further, using the NAVGEM-HA results from 2014 we interpolate the derived amplitudes of all components as well as the mean wind to 92 km and show their variability during the time period of interest between the equator and 60°N in Figure 13. For these results we use the longitude of 279°E to maintain consistency with Figures 9–12. Figures 13a–13c underscore that the week-to-week variability as well as the latitudinal variability of the components at midlatitudes (30°–60°N) is significant.

Figure 14 shows the monthly averaged amplitude versus latitude of all three components for four different years of NAVGEM-HA output available. As with Figure 13, we use the longitude from the active launch site of Cape Canaveral (279°E, see Table 2). Figure 14 serves to indicate that the latitude dependence of 2014 averages are representative of all 4 years of analyzed winds. The derived variability is overplotted as a standard deviation and is similar between the 4 years of NAVGEM-HA output.

In order to more directly address the launch LT dependence of plume transport as indicated by Figures 8b and 15 shows the monthly averaged LT for the maximum of the semi-diurnal (Figure 15a) and diurnal (Figure 15b) components as a function of latitude for 4 years of NAVGEM-HA analyzed winds used in this study. Importantly, the behavior with latitude is largely repeatable from one year to the next near 92 km. The LT of the maximum northward wind at 92 km is on average 4.3 hr for the semi-diurnal tide and 12.0 hr for the diurnal tide from Cape Canaveral to the sub-Arctic.

Figure 16 quantifies the implications of these results to meridional transport over the first 24 hr from Cape Canaveral. The top panel shows meridional winds from the diurnal tide, the semi-diurnal tide, and the superposition of the two. Here we have used average amplitudes and phases for all years and latitudes from the launch site latitude to the sub-Arctic using the results in Figures 14 and 15. In the bottom panel we show the results of a simple parcel advection calculation in the meridional direction using the wind speeds from both components in the top panel. In the bottom panel, the LT represents the starting LT of a parcel over Cape Canaveral. Morning launches at mid-latitudes are in general found to show the most northward motion over 24 hr, which is nearly the same range of LT (23–10 LT) used on the launch record in Figure 8b.

Also overplotted in the bottom panel of Figure 16 is the correlation coefficient as calculated in Figure 8b but for all launch local times, using a sliding 11 hr launch window. One can see not only the prominent peak at 4.5 LT (23–10 LT), but also the shape of the curve is similar to that shown by the calculated average maximum latitude

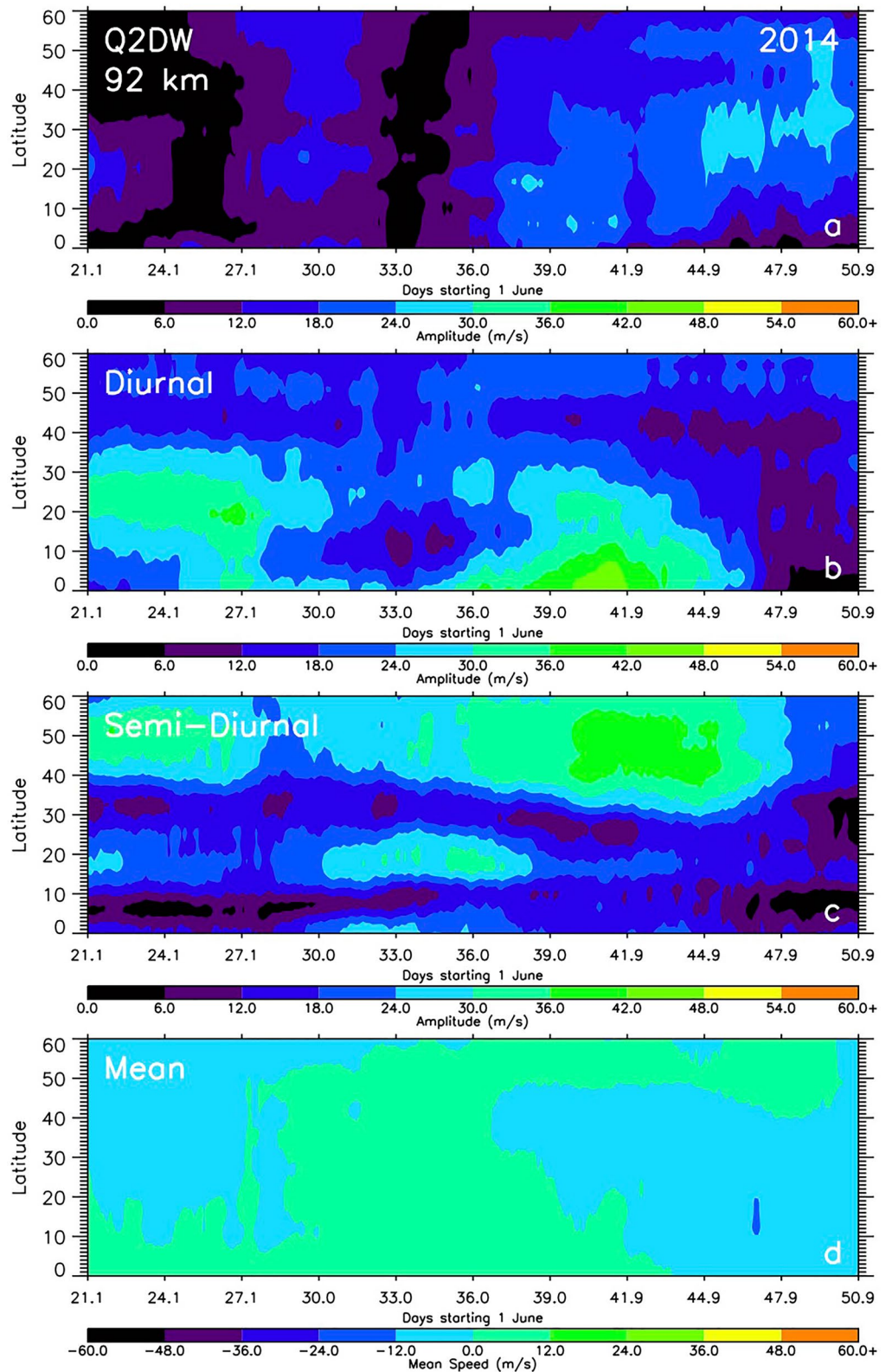


Figure 13. Amplitudes of the fitted components using the 2014 NAVGEM-HA analyzed winds at 92 km and 279°E for the days used in this study.

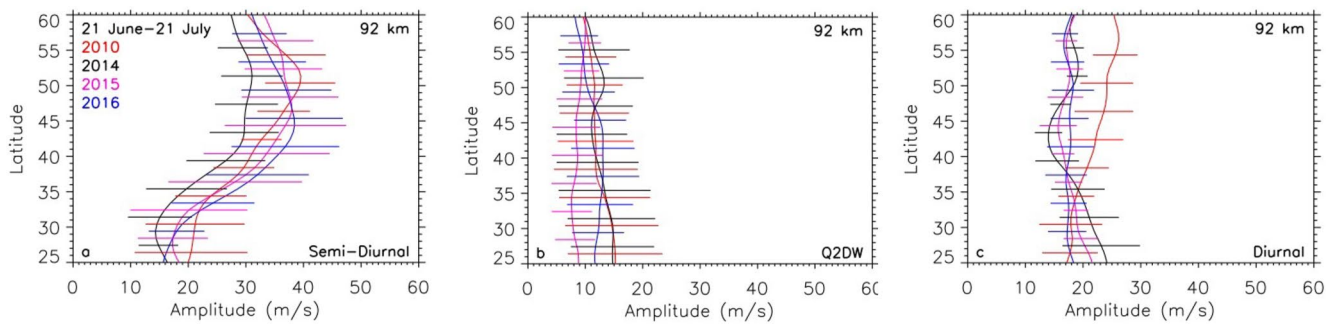


Figure 14. Monthly averaged (21 June to 21 July) amplitudes at 92 km as a function of latitude for (a) the semi-diurnal component, (b) Q2DW, and (c) the diurnal component for all years of NAVGEM-HA analyzed winds. The longitude for the calculations represents Cape Canaveral (279°E). The standard deviation for each year is shown using the same color as the derived amplitude.

from the tidal analysis. There is a noticeable lack of agreement between 0 and 4 LT, but that is likely due to the fact that there are not many launches at this time of day with which to correlate to the cloud frequency time series.

Although Figure 16 shows that morning launch LT yield the most northward motion, additional northward transport is required to reach the sub-Arctic from 29°N. This can be attributed to rapid horizontal spreading of the exhaust plumes. Such rapid spreading was described by Kelley et al. (2009) and later refined by Stevens et al. (2014), who analyzed space shuttle main engine plume observations in the MLT and showed that northward spreading of a shuttle plume can exceed 20° latitude in 24 hr. Using the results from Figure 16 and this rapid diffusive spreading, portions of the plume can typically reach the sub-Arctic in 24 hr from Cape Canaveral after morning launches. Therefore, the LT required to fit the launch record with the CIPS cloud frequency data are consistent with the average tidal phases derived from analyzed meridional winds.

8. Discussion and Summary

We have presented northern mid-latitude mesospheric cloud occurrence frequencies during 2007–2021 from the CIPS instrument on the NASA AIM satellite. These mid-latitude observations are enabled by a new version of the data that quantifies pixel-to-pixel variations in the capability to distinguish between ice cloud and Rayleigh scattering, which are caused by changes in lighting conditions associated with pixel-dependent viewing geometries.

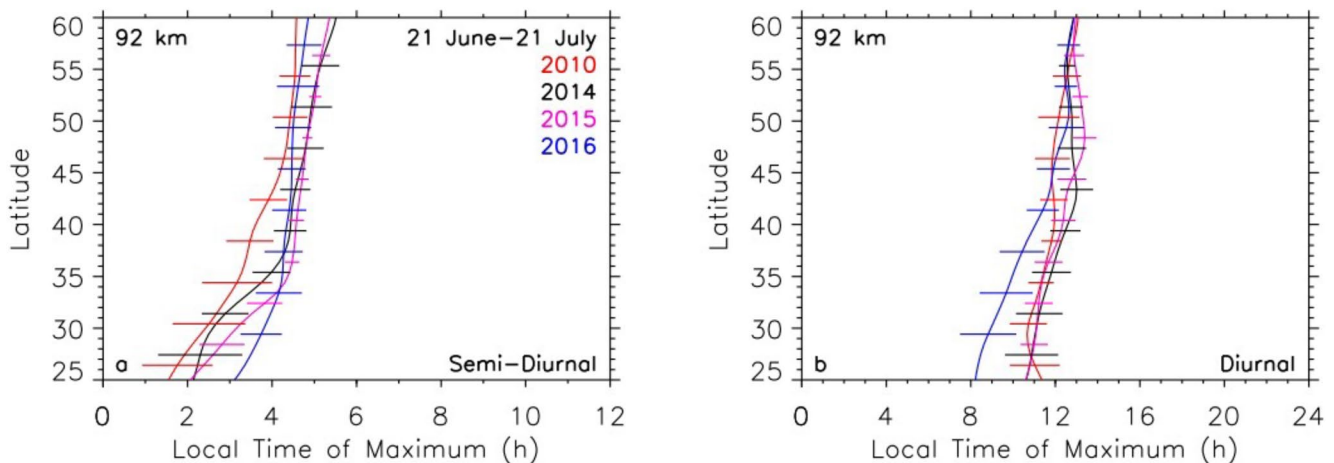


Figure 15. (a) Local time of maximum northward wind for monthly averages of the semi-diurnal tide (21 June to 21 July) at 92 km for the 5 years of analyzed winds used in this study. Results from the longitude of Cape Canaveral (279°E) are given. Standard deviations of the fitted maxima are shown as the horizontal lines in the same color as the year shown. (b) Same as left panel but for the diurnal tide.

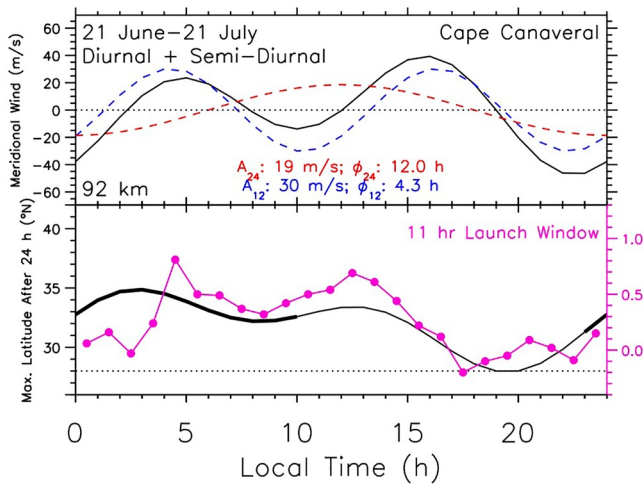


Figure 16. (top panel) Representative diurnal (red dashed) and semi-diurnal (blue dashed) components of meridional wind over Cape Canaveral at 92 km averaged between 21 June and 21 July, where the representative amplitude (A_{24} , A_{12}) and phase (ϕ_{24} , ϕ_{12}) are taken from output in Figures 14 and 15. The sum of the two components is shown in solid black. (bottom panel) The maximum latitude reached after 24 hr as a function of launch local time (LT) from the sum of the two components in the top panel. The heavy black line indicates the LT chosen to select launches contributing to the CIPS frequencies in Figure 8b. The magenta line shows the correlation coefficient (r , right hand axis) between the CIPS frequencies in Figure 8 and the launch record for each LT using a sliding filter that is 11 hr wide and centered on each of the launch LT shown. Dotted line indicates the starting latitude.

Consideration of each pixel's sensitivity to cloud detection allows for a more detailed analysis of the wealth of data available from CIPS at mid-latitudes.

We find that average frequencies were higher in 2018–2021 most likely due to increased sampling during morning LT by CIPS, when lower temperatures lead to more cloud formation. After correcting for the above LT dependence, the frequency time series of sub-Arctic (56°–60°N) mesospheric cloud frequencies from 2007 to 2021 shows no systematic trend during the AIM years of operation and no dependence on the solar cycle.

It is important to note that the generality of our conclusions is likely limited by the high threshold we apply for cloud detection. This means that we are not sampling the entire population of clouds, just the very brightest. Thus, while we emphasize the effects of launch vehicle exhaust, our results are specific to this subset. The effects of interhemispheric coupling from the winter hemisphere on temperatures, and thus cloud formation, at the high latitude summer mesopause have been well documented (Gumbel and Karlsson, 2011; Karlsson et al., 2007, 2009; Siskind et al., 2011; Siskind et al., 2013). The results shown here are not necessarily in disagreement with those earlier studies. Nonetheless, the bright clouds that CIPS detects at these sub-Arctic latitudes are likely drawn from the same population of visible NLC which are observed over populated areas and that receive significant public attention (e.g., Hultgren et al., 2011; Taylor et al., 2002). Thus, it is worthwhile to understand what may drive this fraction of the larger mesospheric cloud population.

With those caveats, we conclude the following for the CIPS mid-latitude mesospheric cloud frequencies:

1. Due to the low mass of the observed clouds (typically less than 2 t/day), space traffic exhaust from launch vehicles advected from lower latitudes can measurably contribute to the observed interannual frequency variability in the sub-Arctic
2. Horizontal winds from a meteorological analysis system between 90 and 95 km suggest that exhaust from a launch in California on 12 June 2019 is responsible for a burst of clouds observed by CIPS and from the ground on 17–18 June over western Europe
3. A parcel advection study for a range of launch LT at mid-latitudes shows that a launch vehicle plume can reach the sub-Arctic in less than 2 days, with a diurnal dependence on the launch LT so that morning launches yield more northward transport
4. The CIPS mid-latitude cloud frequencies in July are strongly correlated with the number of orbital vehicles launched between 23 LT and 10 LT at lower latitudes, indicating that space traffic exhaust helps control the interannual variability of the clouds
5. Tidal analysis of analyzed horizontal winds at 92 km shows that the LT of maximum northward motion is also between about 23 LT and 10 LT at mid-latitudes in July and consistent with the derived LT dependence of the launch record on the CIPS frequencies

The launch LT therefore plays an important role in the ultimate fate of a launch vehicle plume between 90 and 95 km. Quantifying meridional transport of exhaust plumes at higher altitudes (i.e., up to 110 km) necessarily requires a separate analysis since the phases and amplitudes of the migrating tides can change significantly with altitude (e.g., Forbes et al., 1982a; Forbes et al., 1982b; Stober et al., 2020; Zhang et al., 2007).

We note that Siskind et al. (2013) were the first to suggest that the effects of space traffic exhaust on mesospheric clouds might persist beyond the termination of the space shuttle program. Our results support that suggestion. The CIPS data combined with the tidal analysis we present provides evidence that exhaust from northern hemisphere launches not only reaches the sub-Arctic, but likely has a strong influence on the interannual variability of the bright mesospheric clouds observed there.

Data Availability Statement

The CIPS v5.20 L2 data cloud properties and geolocation files used in this study may be found at <https://lasp.colorado.edu/aim/download-data-L2.php>. The NAVGEM-HA and NOGAPS-ALPHA analyses can be found at <https://map.nrl.navy.mil/map/pub/nrl/>. The SHIMMER data may be found at pdf.gsfc.nasa.gov/pub/data/shimmer/pmc_data.

Acknowledgments

Support for this work was provided by the NASA AIM Small Explorer program through Interagency Purchase Request S50029G to N.R.L. and through contract NAS5-03132. SHIMMER was a joint program between the Naval Research Laboratory and the DoD Space Test Program. We thank James Craft and William Barrett for their assistance in processing the CIPS data. The authors thank two anonymous reviewers for comments that improved the manuscript.

References

- Bailey, S. M., Merkel, A. W., Thomas, G. E., & Carstens, J. N. (2005). Observations of polar mesospheric clouds by the Student Nitric Oxide Explorer. *Journal of Geophysical Research*, *110*, D13203. <https://doi.org/10.1029/2004JD005422>
- Broman, L., Benze, S., Gumbel, J., Christensen, O. M., & Randall, C. E. (2019). Common volume satellite studies of polar mesospheric clouds with Odin/OSIRIS tomographs and AIM/CIPS nadir imaging. *Atmospheric Chemistry and Physics*, *19*, 12455–12475. <https://doi.org/10.5194/acp-19-12455-2019>
- Carstens, J. N., Bailey, S. M., Lumpe, J. D., & Randall, C. E. (2013). Understanding uncertainties in the retrieval of polar mesospheric clouds from the Cloud Imaging and Particle Size experiment in the presence of a bright Rayleigh background. *Journal of Atmospheric and Solar-Terrestrial Physics*, *104*, 197–212. <https://doi.org/10.1016/j.jastp.2013.08.006>
- Collins, R. L., Stevens, M. H., Azeem, I., Taylor, M. J., Larsen, M. F., Williams, B. P., et al. (2021). Cloud formation from a localized water release in the upper mesosphere: Indication of rapid cooling. *Journal of Geophysical Research: Space Physics*, *126*, e2019JA027285. <https://doi.org/10.1029/2019JA027285>
- Dalin, P., Perminov, V., Pertsev, N., & Romejko, V. (2020). Updated long-term trends in mesopause temperature, airglow emissions, and noctilucent clouds. *Journal of Geophysical Research: Atmospheres*, *125*, e2019JD030814. <https://doi.org/10.1029/2019jd030814>
- Dalin, P., Pertsev, N., Zadorozhny, A., Connors, M., Schofield, I., Shelton, I., et al. (2008). Ground-based observations of noctilucent clouds with a northern hemisphere network of automatic digital cameras. *Journal of Atmospheric and Solar-Terrestrial Physics*, *70*, 1460–1472. <https://doi.org/10.1016/j.jastp.2008.04.018>
- Dallas, J. A., Raval, S., Alvarez Gaitan, J. P., Saydam, S., & Dempster, A. G. (2020). The environmental impact of emissions from space launches: A comprehensive review. *Journal of Cleaner Production*, *255*, 1–12. <https://doi.org/10.1016/j.jclepro.2020.120209>
- Datta-Barua, S., Pedatella, N., Greer, K., Wang, N., Nutter, L., & Harvey, V. L. (2021). Lower thermospheric material transport via Lagrangian coherent structures. *Journal of Geophysical Research: Space Physics*, *126*, e2020JA028834. <https://doi.org/10.1029/2020JA028834>
- DeLand, M. T., Shettle, E. P., Thomas, G. E., & Olivero, J. J. (2007). Latitude-dependent long-term variations in polar mesospheric clouds from SBUV version 3 PMC data. *Journal of Geophysical Research*, *112*, D10315. <https://doi.org/10.1029/2006JD007857>
- DeLand, M. T., & Thomas, G. E. (2019a). Evaluation of space traffic effects in SBUV polar mesospheric cloud data. *Journal of Geophysical Research: Atmospheres*, *124*, 4203–4221. <https://doi.org/10.1029/2018JD029756>
- DeLand, M. T., & Thomas, G. E. (2019b). Extending the SBUV PMC data record with OMPS NP. *Atmospheric Chemistry and Physics*, *19*, 7913–7925. <https://doi.org/10.5194/acp-19-7913-2019>
- Drob, D. P., Emmert, J. T., Meriwether, J. W., Makela, J. J., Doornbos, E., Conde, M., et al. (2015). An update to the Horizontal Wind Model (HWM): The quiet time thermosphere. *Earth and Space Science*, *2*, 301–319. <https://doi.org/10.1002/2014ea000089>
- Dubietis, A., Dalin, P., Balčiūnas, R., & Černis, K. (2010). Observations of noctilucent clouds from Lithuania. *Journal of Atmospheric and Solar-Terrestrial Physics*, *72*, 1090–1099. <https://doi.org/10.1016/j.jastp.2010.07.004>
- Eckermann, S. D., Hoppel, K. W., Coy, L., McCormack, J. P., Siskind, D. E., Nielsen, K., et al. (2009). High-altitude data assimilation system experiments for the northern summer mesosphere season of 2007. *Journal of Atmospheric and Solar-Terrestrial Physics*, *71*, 531–551. <https://doi.org/10.1016/j.jastp.2008.09.036>
- Englert, C. R., Stevens, M. H., Siskind, D. E., Harlander, J. M., & Roesler, F. L. (2010). Spatial Heterodyne Imager for Mesospheric Radicals on STPSat-1. *Journal of Geophysical Research*, *115*, D20306. <https://doi.org/10.1029/2010jd014398>
- Forbes, J. M. (1982a). Atmospheric tides 1. Model description and results for the solar diurnal component. *Journal of Geophysical Research*, *87*, 5222–5240. <https://doi.org/10.1029/ja087ia07p05222>
- Forbes, J. M. (1982b). Atmospheric tides 2. The solar and lunar semidiurnal components. *Journal of Geophysical Research*, *87*, 5241–5252. <https://doi.org/10.1029/ja087ia07p05241>
- Forbes, J. M. (1995). *Tidal and planetary waves. In The upper mesosphere and lower thermosphere: A review of experiment and theory (Geophysical Monograph 87)*. American Geophysical Union.
- Gadsden, M. (1998). The north-west Europe data on noctilucent clouds: A survey. *Journal of Atmospheric and Solar-Terrestrial Physics*, *60*, 1163–1174. [https://doi.org/10.1016/s1364-6826\(98\)00072-8](https://doi.org/10.1016/s1364-6826(98)00072-8)
- Gerding, M., Baumgarten, G., Zecha, M., Lübken, F.-J., & Baumgarten, K. (2021). On the unusually bright and frequent noctilucent clouds in summer 2019 above Northern Germany. *Journal of Atmospheric and Solar-Terrestrial Physics*, *217*, 1–12. <https://doi.org/10.1016/j.jastp.2021.105577>
- Gerding, M., Hoffner, J., Hoffmann, P., Kopp, M., & Lübken, F.-J. (2013). Noctilucent cloud variability and mean parameters from 15 years of lidar observations at a mid-latitude site (54 N, 12 E). *Journal of Geophysical Research: Atmospheres*, *118*, 317–328. <https://doi.org/10.1029/2012JD018319>
- Gumbel, J., & Karlsson, B. (2011). Intra- and inter-hemispheric coupling effects on the polar summer mesosphere. *Geophysical Research Letters*, *38*, L14804. <https://doi.org/10.1029/2011GL047968>
- Hervig, M. E., Gerding, M., Stevens, M. H., Stockwell, R., Bailey, S. M., Russell, J. M. III, & Stober, G. (2016). Mid-latitude mesospheric clouds and their environment from SOFIE observations. *Journal of Atmospheric and Solar-Terrestrial Physics*, *149*, 1–14. <https://doi.org/10.1016/j.jastp.2016.09.004>
- Hervig, M. E., Siskind, D. E., Bailey, S. M., Merkel, A. W., DeLand, M. T., & Russell, J. M. III (2019). The missing solar cycle response of the polar summer mesosphere. *Geophysical Research Letters*, *46*, 10132–10139. <https://doi.org/10.1029/2019gl083485>
- Hervig, M. E., Stevens, M. H., Gordley, L. L., Deaver, L. E., Russell, J. M. III, & Bailey, S. M. (2009). Relationships between polar mesospheric clouds, temperature, and water vapor from Solar Occultation for Ice Experiment (SOFIE) observations. *Journal of Geophysical Research*, *114*, D20203. <https://doi.org/10.1029/2009jd012302>

- Hoppel, K. W., Baker, N. L., Coy, L., Eckermann, S. D., McCormack, J. P., Nedoluha, G. E., & Siskind, D. E. (2008). Assimilation of stratospheric and mesospheric temperatures from MLS and SABER into a global NWP model. *Atmospheric Chemistry and Physics*, 8, 6103–6116. <https://doi.org/10.5194/acp-8-6103-2008>
- Hoppel, K. W., Eckermann, S. D., Coy, L., Nedoluha, G. E., Allen, D. R., Swadley, S. D., & Baker, N. L. (2013). Evaluation of SSMIS upper atmosphere sounding channels for high-altitude data assimilation. *Monthly Weather Review*, 141, 3314–3330. <https://doi.org/10.1175/mwr-d-13-00003.1>
- Hultgren, K., Körnich, H., Gumbel, J., Gerding, M., Hoffmann, P., Lossow, S., & Megner, L. (2011). What caused the exceptional mid-latitude noctilucent cloud event in July 2009? *Journal of Atmospheric and Solar-Terrestrial Physics*, 73, 2125–2131. <https://doi.org/10.1016/j.jastp.2010.12.008>
- Karlsson, B., Körnich, H., & Gumbel, J. (2007). Evidence for interhemispheric stratosphere-mesosphere coupling derived from noctilucent cloud properties. *Geophysical Research Letters*, 34, L16806. <https://doi.org/10.1029/2007GL030282>
- Karlsson, B., Randall, C. E., Benze, S., Mills, M., Harvey, V. L., Bailey, S. M., & Russell, J. M. III (2009). Intra-seasonal variability of polar mesospheric clouds due to inter-hemispheric coupling. *Geophysical Research Letters*, 36, L20802. <https://doi.org/10.1029/2009GL040348>
- Kelley, M. C., Nicolls, M. J., Varney, R. H., Collins, R. L., Doe, R., Plane, J. M. C., et al. (2010). Radar, lidar, and optical observations in the polar summer mesosphere shortly after a space shuttle launch. *Journal of Geophysical Research*, 115, A05304. <https://doi.org/10.1029/2009JA014938>
- Kelley, M. C., Seyler, C. E., & Larsen, M. F. (2009). Two-dimensional turbulence, space shuttle plume transport in the thermosphere, and a possible relation to the Great Siberian impact event. *Geophysical Research Letters*, 36, L14103. <https://doi.org/10.1029/2009GL038362>
- Kirkwood, S., Dalin, P., & Réchou, A. (2008). Noctilucent clouds observed from the UK and Denmark – Trends and variations over 43 years. *Annales de Geophysicae*, 26, 1243–1254. <https://doi.org/10.5194/angeo-26-1243-2008>
- Kuhl, D. D., Rosmond, T. E., Bishop, C. H., McLay, J., & Baker, N. L. (2013). Comparison of hybrid ensemble/4DVar and 4DVar within the NAVDAS-AR data assimilation Framework. *Monthly Weather Review*, 141, 2740–2758. <https://doi.org/10.1175/mwr-d-12-00182.1>
- Larson, E. J. L., Portmann, R. W., Rosenlof, K. H., Fahey, D. W., Daniel, J. S., & Ross, M. N. (2017). Global atmospheric response to emissions from a proposed reusable space launch system. *Earth's Future*, 5, 37–48. <https://doi.org/10.1002/2016EF000399>
- Lieberman, R. S., Riggan, D. M., Orland, D. A., Oberheide, J., & Siskind, D. E. (2015). Global observations and modeling of nonmigrating diurnal tides generated by tide-planetary wave interactions. *Journal of Geophysical Research: Atmospheres*, 120, 11419–11437. <https://doi.org/10.1002/2015JD023739>
- Liu, H.-L. (2007). On the large wind shear and fast meridional transport above the mesopause. *Geophysical Research Letters*, 34, L08815. <https://doi.org/10.1029/2006GL028789>
- Lumpe, J. D., Bailey, S. M., Carstens, J. N., Randall, C. E., Rusch, D. W., Thomas, G. E., et al. (2013). Retrieval of polar mesospheric cloud properties from CIPS: Algorithm description, error analysis and cloud detection sensitivity. *Journal of Atmospheric and Solar-Terrestrial Physics*, 104, 167–196. <https://doi.org/10.1016/j.jastp.2013.06.007>
- Machol, J., Snow, M., Woodraska, D., Woods, T., Viereck, R., & Coddington, O. (2019). An improved Lyman-alpha composite. *Earth and Space Science*, 6, 2263–2272. <https://doi.org/10.1029/2019EA000648>
- McClintock, W. E., Rusch, D. W., Thomas, G. E., Merkel, A. W., Lankton, M. R., Drake, V. A., et al. (2009). The cloud imaging and particle size experiment on the Aeronomy of Ice in the mesosphere mission: Instrument concept, design, calibration, and on-orbit performance. *Journal of Atmospheric and Solar-Terrestrial Physics*, 71, 340–355. <https://doi.org/10.1016/j.jastp.2008.10.011>
- McCormack, J., Hoppel, K., Kuhl, D., De Wit, R., Stober, G., Espy, P., et al. (2017). Comparison of mesospheric winds from a high-altitude meteorological analysis system and meteor radar observations during the boreal winters of 2009–2010 and 2012–2013. *Journal of Atmospheric and Solar-Terrestrial Physics*, 154, 132–166. <https://doi.org/10.1016/j.jastp.2016.12.007>
- McCormack, J. P., Coy, L., & Singer, W. (2014). Intra-seasonal and inter-annual variability of the quasi 2 day wave in the Northern Hemisphere summer mesosphere. *Journal of Geophysical Research*, 119, 2928–2946. <https://doi.org/10.1002/2013JD020199>
- Meier, R. R., Plane, J. M. C., Stevens, M. H., Paxton, L. J., Christensen, A. B., & Crowley, G. (2010). Can molecular diffusion explain Space Shuttle plume spreading? *Geophysical Research Letters*, 37, L08101. <https://doi.org/10.1029/2010GL042868>
- Meier, R. R., Stevens, M. H., Plane, J. M. C., Emmert, J. T., Crowley, G., Azeem, I., et al. (2011). A study of space shuttle plumes in the lower thermosphere. *Journal of Geophysical Research*, 116, A12322. <https://doi.org/10.1029/2011JA016987>
- Niciejewski, R., Skinner, W., Cooper, M., Marshall, A., Meier, R. R., Stevens, M. H., et al. (2011). Verification of large-scale rapid transport in the lower thermosphere: Tracking the exhaust plume of STS-107 from launch to the Antarctic. *Journal of Geophysical Research*, 116, A05302. <https://doi.org/10.1029/2010JA016277>
- Oberheide, J., Forbes, J. M., Häusler, K., Wu, Q., & Bruinsma, S. L. (2009). Tropospheric tides from 80 to 400 km: Propagation, interannual variability, and solar cycle effects. *Journal of Geophysical Research*, 114, D00105. <https://doi.org/10.1029/2009JD012388>
- Pertsev, N., Dalin, P., Perminov, V., Romejko, V., Dubietis, A., Balčiunas, R., et al. (2014). Noctilucent clouds observed from the ground: Sensitivity to mesospheric parameters and long-term time series. *Planets and Space*, 66, 98. <https://doi.org/10.1186/1880-5981-66-98>
- Pokhotelov, D., Stober, G., & Chau, J. L. (2019). Statistical climatology of mid-latitude mesospheric summer echoes characterized by OSWIN (Ostee-Wind) radar observations. *Atmospheric Chemistry and Physics*, 19, 5251–5258. <https://doi.org/10.5194/acp-19-5251-2019>
- Russell, J. M. III, Bailey, S. M., Gordley, L. L., Rusch, D. W., Horányi, M., Hervig, M. E., et al. (2009). The aeronomy of ice in the mesosphere (AIM) mission: Overview and early science results. *Journal of Atmospheric and Solar-Terrestrial Physics*, 71, 289–299. <https://doi.org/10.1016/j.jastp.2008.08.011>
- Russell, J. M. III, Rong, P., Hervig, M. E., Siskind, D. E., Stevens, M. H., Bailey, S. M., & Gumbel, J. (2014). Analysis of northern midlatitude noctilucent cloud occurrences using satellite data and modeling. *Journal of Geophysical Research: Atmospheres*, 119, 3238–3250. <https://doi.org/10.1002/2013JD021017>
- Schmidt, F., Baumgarten, G., Berger, U., Fiedler, J., & Lübken, F.-J. (2018). Local time dependence of polar mesospheric clouds: A model study. *Atmospheric Chemistry and Physics*, 18, 8893–8908. <https://doi.org/10.5194/acp-18-8893-2018>
- Siskind, D. E., Drob, D. P., Dymond, K. F., & McCormack, J. P. (2014). Simulations of the effects of vertical transport on the thermosphere and ionosphere using two coupled models. *Journal of Geophysical Research: Space Physics*, 119, 1172–1185. <https://doi.org/10.1002/2013JA019116>
- Siskind, D. E., Drob, D. P., Emmert, J. T., Stevens, M. H., Sheese, P. E., Llewellyn, E. J., et al. (2012). Linkages between the cold summer mesopause and thermospheric zonal mean circulation. *Geophysical Research Letters*, 39, L01804. <https://doi.org/10.1029/2011GL050196>
- Siskind, D. E., Stevens, M. H., Emmert, J. T., Drob, D. P., Kochenash, A. J., Russell, J. M. III, et al. (2003). Signatures of shuttle and rocket exhaust plumes in TIMED/SABER radiance data. *Geophysical Research Letters*, 30, 1819. <https://doi.org/10.1029/2003GL017627>
- Siskind, D. E., Stevens, M. H., Hervig, M., Sassi, F., Hoppel, K., Englert, C. R., & Kochenash, A. J. (2011). Consequences of recent Southern Hemisphere winter variability on polar mesospheric clouds. *Journal of Atmospheric and Solar-Terrestrial Physics*, 73, 2013–2021. <https://doi.org/10.1016/j.jastp.2011.06.014>

- Siskind, D. E., Stevens, M. H., Hervig, M. E., & Randall, C. E. (2013). Recent observations of high mass density polar mesospheric clouds: A link to space traffic? *Geophysical Research Letters*, *40*, 2813–2817. <https://doi.org/10.1002/grl.50540>
- Stevens, M. H., Englert, C. R., DeLand, M. T., & Hervig, M. (2005a). The polar mesospheric cloud mass in the Arctic summer. *Journal of Geophysical Research*, *110*, A02306. <https://doi.org/10.1029/2004JA010566>
- Stevens, M. H., Englert, C. R., Hervig, M., Petelina, S. V., Singer, W., & Nielsen, K. (2009). The diurnal variation of polar mesospheric cloud frequency near 55°N observed by SHIMMER. *Journal of Atmospheric and Solar-Terrestrial Physics*, *71*, 401–407. <https://doi.org/10.1016/j.jastp.2008.10.009>
- Stevens, M. H., Gumbel, J., Englert, C. R., Grossmann, K. U., Rapp, M., & Hartogh, P. (2003). Polar mesospheric clouds formed from space shuttle exhaust. *Geophysical Research Letters*, *30*, 1546. <https://doi.org/10.1029/2003GL017249>
- Stevens, M. H., Lieberman, R. S., Siskind, D. E., McCormack, J. P., Hervig, M. E., & Englert, C. R. (2017). Periodicities of polar mesospheric clouds inferred from a meteorological analysis and forecast system. *Journal of Geophysical Research: Atmospheres*, *122*, 4508–4527. <https://doi.org/10.1002/2016JD025349>
- Stevens, M. H., Lossow, S., Fiedler, J., Baumgarten, G., Lübken, F.-J., Hallgren, K., et al. (2012). Bright polar mesospheric clouds formed by main engine exhaust from the space shuttle's final launch. *Journal of Geophysical Research*, *117*, D19206. <https://doi.org/10.1029/2012JD017638>
- Stevens, M. H., Lossow, S., Siskind, D. E., Meier, R. R., Randall, C. E., Russell, J. M. III, et al. (2014). Space shuttle exhaust plumes in the lower thermosphere: Advective transport and diffusive spreading. *Journal of Atmospheric and Solar-Terrestrial Physics*, *108*, 50–60. <https://doi.org/10.1016/j.jastp.2013.12.004>
- Stevens, M. H., Meier, R. R., Chu, X., DeLand, M. T., & Plane, J. M. C. (2005b). Antarctic mesospheric clouds formed from space shuttle exhaust. *Geophysical Research Letters*, *32*, L13810. <https://doi.org/10.1029/2005GL023054>
- Stevens, M. H., Siskind, D. E., Eckermann, S. D., Coy, L., McCormack, J. P., Englert, C. R., et al. (2010). Tidally induced variations of polar mesospheric cloud altitudes and ice water content using a data assimilation system. *Journal of Geophysical Research*, *115*, D18209. <https://doi.org/10.1029/2009JD013225>
- Stober, G., Baumgarten, K., McCormack, J. P., Brown, P., & Czarniecki, J. (2020). Comparative study between ground-based observations and NAVGEM-HA analysis data in the mesosphere and lower thermosphere region. *Atmospheric Chemistry and Physics*, *20*, 11979–12010. <https://doi.org/10.5194/acp-20-11979-2020>
- Taylor, M. J., Gadsden, M., Lowe, R. P., Zalcik, M. S., & Brausch, J. (2002). Mesospheric cloud observations at unusually low latitudes. *Journal of Atmospheric and Solar-Terrestrial Physics*, *64*, 991–999. [https://doi.org/10.1016/s1364-6826\(02\)00053-6](https://doi.org/10.1016/s1364-6826(02)00053-6)
- Wang, N., Ramirez, U., Flores, F., & Datta-Barua, S. (2017). Lagrangian coherent structures in the thermosphere: Predictive transport barriers. *Geophysical Research Letters*, *44*, 4549–4557. <https://doi.org/10.1002/2017GL072568>
- Wu, Q., Ortland, D. A., Killeen, T. L., Roble, R. G., Hagan, M. E., Liu, H.-L., et al. (2008a). Global distribution and interannual variations of mesospheric and lower thermospheric neutral wind diurnal tide: 1. Migrating tide. *Journal of Geophysical Research*, *113*, A05308. <https://doi.org/10.1029/2007JA012542>
- Wu, Q., Ortland, D. A., Killeen, T. L., Roble, R. G., Hagan, M. E., Liu, H.-L., et al. (2008b). Global distribution and interannual variations of mesospheric and lower thermospheric neutral wind diurnal tide: 2. Nonmigrating tide. *Journal of Geophysical Research*, *113*, A05309. <https://doi.org/10.1029/2007JA012543>
- Wu, Q., Ortland, D. A., Solomon, S. C., Skinner, W. R., & Niciejewski, R. J. (2011). Global distribution, seasonal, and inter-annual variations of mesospheric semidiurnal tide observed by TIMED TIDI. *Journal of Atmospheric and Solar-Terrestrial Physics*, *73*, 2482–2502. <https://doi.org/10.1016/j.jastp.2011.08.007>
- Yue, J., & Liu, H.-L. (2010). Fast meridional transport in the lower thermosphere by planetary-scale waves. *Journal of Atmospheric and Solar-Terrestrial Physics*, *72*, 1372–1378. <https://doi.org/10.1016/j.jastp.2010.10.001>
- Yue, J., Liu, H.-L., Meier, R. R., Chang, L., Gu, S.-Y., & Russell, J. M. III (2013). On the fast zonal transport of the STS-121 space shuttle exhaust plume in the lower thermosphere. *Journal of Atmospheric and Solar-Terrestrial Physics*, *94*, 19–27. <https://doi.org/10.1016/j.jastp.2012.12.017>
- Zhang, S. P., McLandress, C., & Shepherd, G. G. (2007). Satellite observations of mean winds and tides in the lower thermosphere: 2. Wind Imaging Interferometer monthly winds for 1992 and 1993. *Journal of Geophysical Research*, *112*, D21105. <https://doi.org/10.1029/2007JD008457>